Understanding and Enhancing the Cycling Stability of Layered Double Hydroxides with Intercalated Ferrocene Anions for Energy Storage Application

Patrick Gerlach,*[a, b] Camille Douard,[a, b] Julien Sarmet,[c] Fabrice Leroux,[c] Christine Tavoit-Gueho,[c] Philippe Stevens,[b, d] Gwenaëlle Toussaint,[b, d] and Thierry Brousse*[a, b]

In this work, the layered double hydroxide (LDH) $Mg_2Al(OH)_6$ was intercalated with redox active ferrocene carboxylate anions in order to implement charge storage capability to the interlayer spaces of the LDH structure. Two sets of anions, namely mono- and dicarboxylic ferrocene, were intercalated to produce two different active materials: MgAl-FcMono and MgAl-FcDi. The electrochemical investigation of these two materials was performed in two model electrolytes: 1 M LiTFSI in H_2O and $Pyr_{13}TFSI$. In the aqueous electrolyte, the first charge reaches the full theoretic capacity of ca. 60 and 40 mAh g^{-1} for both materials. However, significantly less capacity is stored and delivered during subsequent cycles. In-situ UV/vis experiments identified the loss as a release of charged ferrocene anions from the LDH during oxidation in the charging process, which is more severe for MgAl-FcMono. It is possible to prevent this release of redox species by the use of the ionic liquid $Pyr_{13}TFSI$ as a high concentrated electrolyte. Subsequently, both materials cycled very steadily with high coulombic efficiency for 150 cycles. This better understanding of the capacity degradation of the LDH-ferrocene active material is key to improving this new and promising concept of using modified LDHs as active material in energy storage application.

1. Introduction

Layered double hydroxides (LDHs) are brucite-type ($Mg(OH)_2$) layered materials, that can be described with the general formula $[M^{2+}_{1-x}M^{3+}_x(OH)_2]^{z+}(A^{n-})_{z/n}\cdot y\cdot H_2O$, where M^{2+} and M^{3+} are divalent and trivalent metals cations and A^{n-} describes intercalated anions between the metal hydroxide layers.[1–7] The latter consists of edge-sharing metal hydroxide octahedra $M(OH)_6$ in which a partial substitution of divalent by trivalent cations (represented by x) produces an excess of positive charge in the layers that is compensated by the presence of anions between the layers. A common and well known example in nature for this structure is hydrotalcite $[Mg_6Al_2(OH)_{16}]CO_3$ x 4 H_2O (x = 0.25).[8,9]

The current interest in LDHs relies upon several properties, and especially on their compositional diversity for both the cations in the hydroxide layers and the interlayer anions. The Mg/Al couple in the LDH layers has been the most widely studied, but these cations can be substituted by many others, such as Zn, Co, Ni, Mn, and Fe as divalent cations and Cr, Co, Fe, V, Mn, Ga, as trivalent cations. Similarly, a great variety of anions can be intercalated, including inorganic and organic anions, coordination compounds, polyoxometalates, and biomolecules.[10] They have been used in many applications like ion exchange,[11–13] drug delivery,[14–17] water purification,[18–21] polymer[22–24] or anti corrosion[25–28] additives, sensors[29–34] and catalysis.[35–49] LDHs have also been investigated in energy storage application[50] as battery[51–63] and supercapacitor-type electrode materials.[64–76] In batteries, using a faradic reaction, the charge storage mechanism uses a change in oxidation state of the metal cations in the hydroxide layers.

A very recent example of the utilization of LDHs in an asymmetric supercapacitor (hybrid device) is given by Yao et al. with the use of a Mg doped Co—Ni LDH confined in mesoporous carbon.[77] When used with a classical activated carbon electrode, this LDH storage device reached an energy density of 41 Wh kg^{-1} at 800 W kg^{-1} and provided a capacity retention of 91 % after 30,000 cycles at 10 A g^{-1}.

As an aside, the authors would like to highlight that when charge storage mechanism in LDH-based electrodes involves a redox reaction, the capacity needs to expressed in mAh g^{-1} or in Coulombs and not in Farads.[78]

[a] P. Gerlach, C. Douard, T. Brousse
Nantes Université, CNRS, Institut des Matériaux de Nantes Jean Rouxel, IMN, 2 rue de la Houssinière, BP32229, CEDEX 3, F-44322 Nantes, France
E-mail: thierry.brousse@univ-nantes.fr
        patrick.gerlach@cnrs-imn.fr

[b] P. Gerlach, C. Douard, P. Stevens, G. Toussaint, T. Brousse
Réseau sur le Stockage Electrochimique de l'Energie (RS2E), CNRS FR 3459, 33 rue Saint Leu, CEDEX, F-80039 Amiens, France

[c] J. Sarmet, F. Leroux, C. Tavoit-Gueho
Université Clermont Auvergne, Institut de Chimie de Clermont-Ferrand (ICCF), UMR n°6296, Clermont Auvergne INP, CNRS, Institut Pascal, F-63000 Clermont-Ferrand, France

[d] P. Stevens, G. Toussaint
EDF R&D, Department LME, Avenue des Renardières, CEDEX, F-77818 Moret-sur-Loing, France

In the work of He *et al* for example, a CoAl-LDH cathode in combination with a zinc foil anode was used.[61] In their study, the CoAl-LDH system was able to outperform a classical $Co(OH)_2$ electrode and the cell provided a maximum energy density of 393 $Wh\,kg^{-1}$ at 2.2 $kW\,kg^{-1}$ and a maximum power density of 76 $kW\,kg^{-1}$ at 264 $Wh\,kg^{-1}$. Furthermore, 8000 cycles with a capacity retention of 96% at a current density of 10 $A\,g^{-1}$ was achieved.

In these examples, LDH active materials were able to present a good performance for energy storage application by the utilization of the redox sites (metal cations) directly present within the LDH layers, which leads consequently to changes in the structure of the LDHs.

Another strategy consists in using the LDH as a matrix for intercalating anionic redox active species. Mousty et. al. were the first to show in 1994 that redox active anions can be intercalated into LDHs to produce biosensor or electro catalyst materials.[34,79,80] In more recent work, we showed that redox active anions like anthraquinone sulfonate, riboflavin phosphate or ferrocene carboxylate intercalated in LDH layers, display a redox activity that can be used in electrochemical energy storage application using an aqueous electrolyte.[81,82] By involving both the cationic layers as well as the interlayer space of the LDH electrode materials for energy storage, this approach can lead to further enhancement of the specific capacity of LDH based electrodes. However, in all of these studies very limited cycling stability has been depicted. In the case of anthraquinone sulfonate intercalated in a $Mg_2Al(OH)_6$ LDH, dissolution of the intercalated redox active anthraquinone anions into the aqueous electrolyte was observed which resulted in a rapid loss of specific capacity during cycling.[82] There, the dissolution was described as intrinsic since the charge imbalance in the LDH structure after reduction forces the anions to leave the electrode.

In the continuation of these studies, this work aims to improve the cycling stability of LDHs intercalated with redox active organic anions. This objective is approached in two ways. First we tried to clarify the influence of the valence of the intercalated redox active organic anions on the release of the active anions from the electrode as previously reported[81,82] and

therewith the cycling stability of the active material. Then the possible influence of the electrolyte media on the release phenomenon and subsequently on the cycling stability was investigated.

To achieve this objective, mono- and dicarboxylic ferrocene anions were intercalated in the structure of a $Mg_2Al(OH)_6$ x 2 H_2O LDH leading to two model LDH electrode materials with the ideal formulas $Mg_2Al(OH)_6[FcMono]_{1.0}$ x 2 H_2O and $Mg_2Al(OH)_6[FcDi]_{0.5}$ x 2 H_2O. In both cases the substitution factor x is 0.33 (with regard to the general formula $[M^{2+}_{1-x}M^{3+}_x(OH)_2]^{z+}(A^{n-})_{z/n}$ y H_2O) which corresponds to the largest AEC (anionic exchange capacity); hence the largest amount of electroactive anions that can be intercalated. The structures of the newly synthesized LDH materials are shown in Figure 1. A more detailed representation of the structure can be found in the supplementary information S1.

For the sake of simplicity, these materials are labelled MgAl-FcMono and MgAl-FcDi. Composite electrodes prepared from these two materials were tested in two different electrolytes, an aqueous electrolyte 1 M Lithium bis(trifluoromethanesulfonyl)imide (LiTFSI) in H_2O and an electrolyte composed of a pure ionic liquid (IL), N-propyl-N-methylpyrrolidinium bis(trifluoromethanesulfonyl)imide (Pyr_{13}TFSI).

Ferrocene has been widely investigated as an organic redox active group,[83] as an electrode potential marker in cyclic voltammetry,[84–89] and as an active material in organic battery electrode materials[90–92] or in redox-flow energy storage.[93–97] In these applications, it displays a standard electrode potential of +0.4 V vs. NHE.[98]

The change in the valence state of the intercalated ferrocene carboxylate results in two major differences in the structures of MgAl-FcMono and MgAl-FcDi. First, due to the divalent charge of the dicarboxylic ferrocene anions, only half the amount of anions in comparison to monocarboxylic ferrocene anions is necessary to compensate the positive charge of $[Mg_2Al(OH)_6]^+$ layers leading ideally to 0.5 FcDi anions per formula unit, which is represented in the formula $Mg_2Al(OH)_6[FcDi]_{0.5}$ x 2 H_2O. On the other hand 1 FcMono anions per
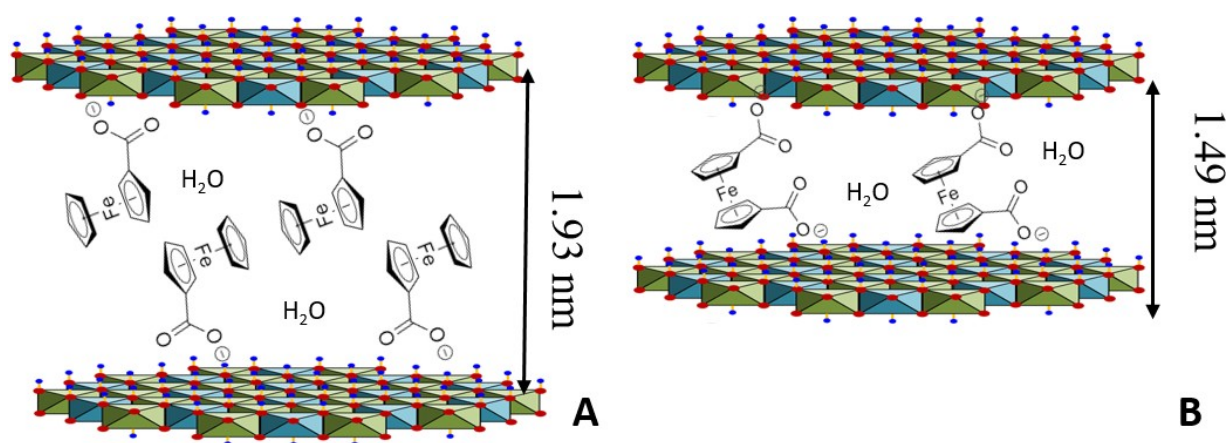

Figure 1. Schematic representation of the structure of A) MgAl-FcMono and B) MgAl-FcDi.

Batteries & Supercaps

Research Article
doi.org/10.1002/batt.202400256

Chemistry
Europe
European Chemical
Societies Publishing

formula unit are needed for charge compensation and results to $Mg_2Al(OH)_6[FcMono]_{1.0}$ x 2 H_2O.

Secondly, the position of anionic groups of the intercalated ferrocene anions leads to two different configurations of the anions in the structure. While in the case of FcMono, an alternating up and down antiparallel arrangement is obtained (Figure 1), a more compact is displayed with FcDi, where the position of carboxylate groups at both ends of the anion leads to a monolayer interlayer arrangement and thus to a more compact structure (Figure 1B).–1

Finally, the different numbers of intercalated anions in MgAl-FcMono and MgAl-FcDi result in different theoretical specific capacities Q_{th} calculated with Equation (1):

$$Q_{th} = \frac{z \times F}{M \times 3.6} \tag{1}$$

Where z is the number of exchanged electrons ($z = 1$ for MgAl-FcMono and 0.5 for MgAl-FcDi), F is the Faraday constant ($F = 9.65 \times 10^4$ $C\,mol^{-1}$) and M is the molar mass of MgAl-FcMono and MgAl-FcDi ($M_{Mono} = 443$ $g\,mol^{-1}$ and 350 $g\,mol^{-1}$ M_{Di}). For the calculation 1 mol of $FcCO_2^-$ were assumed per mol of $[Mg_2Al-(OH)_6]^+$ x 2 H_2O in MgAl-FcMono and 0.5 mol of $Fc(CO_2)_2^{2-}$ in 1 mol MgAl-FcDi. This results to a theoretical capacity of 60.5 $mAh\,g^{-1}$ for MgAl-FcMono and 38 $mAh\,g^{-1}$ for MgAl-FcDi. The practical capacity of the electrode materials were determined in the results part.

2. Results and Discussion

The XRD patterns of MgAl-FcMono and MgAl-FcDi samples displayed in Figure 2A present diffraction peaks that can be interpreted by a series of a large number of (00 l) and (0kl)/(hk0) diffraction peaks, which can be indexed in the rhombohedral space group R-3 m, typical for LDH-based systems. The interlayer distances calculated from the position of (003) diffraction peaks i.e. d~1.93 nm for MgAl-FcMono and d~1.49 nm for MgAl-FcDi indicate a bilayer and a monolayer arrangement of interlayer ferrocene molecules respectively as reported elsewhere.[79,81] The difference is due to the presence of two carboxylate groups for FcDi molecule in para configuration leading to an interaction on both sides with the hydroxide sheets. The interlayer arrangement is less constrained with FcMono bearing one carboxylate group.

The chemical compositions given in Table 1 were obtained by combining CNSH/ICP and TGA analysis (Figure 2B) of the bulk powders and EDX analysis of individual crystals. To achieve a total balance of the charges, we considered the co-intercalation of carbonate anions which is very likely and quite common in LDH materials.[99] These experimental compositions agree well with the expected formulas and confirm the high purity and homogeneity of the prepared powders. However, small differences of the real structures with respect to the ideal ones can be depicted. Specifically the amount of intercalated H_2O molecules results to 3.6 per unit for both materials, which is higher than expected. This affects the real molar mass and therewith the theoretical capacity. The formula $Mg_2Al-(OH)_6[FcMono]_{1.0}$ x 3.6 H_2O instead of $Mg_2Al(OH)_6[FcMono]_{1.0}$ x 2 H_2O yields to a molar mass of 472.5 $g\,mol^{-1}$ with a theoretical capacity of 56.7 $mAh\,g^{-1}$. $Mg_2Al(OH)_6[FcDi]_{0.5}$ x 2.4 H_2O instead of $Mg_2Al(OH)_6[FcDi]_{0.5}$ x 2 H_2O,on the other hand, yields to 357 $g\,mol^{-1}$ and thus 37.5 $mAh\,g^{-1}$.

Figure 2C shows infrared measurements of the single anions of FcMono and Di as well as the signals of MgAl-FcMono and MgAl-FcDi. There, the broad and intense band around 3450 cm^{-1} corresponds to the vibration of the hydroxyl groups $\nu(OH)$ in the layer and the water molecules adsorbed and intercalated between the layers. The absorption band around 1600 cm^{-1} corresponds to the deformation band of the water molecules $\delta(H_2O)$. Their intensities are related to the degree of hydration of the compound.
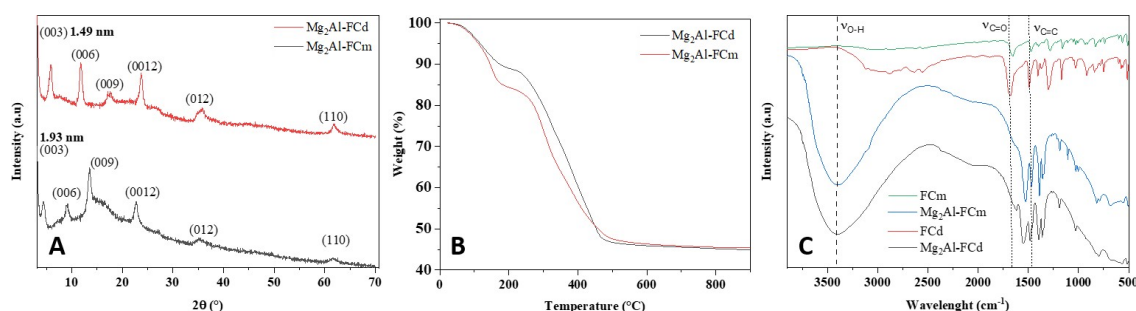

Figure 2. (A) XRD (B) TGA and (C) Infrared spectrum of MgAl-FcMono and MgAl-FcDi.

Table 1. Chemical composition of MgAl-FcMono and MgAl-FcDi obtained from ICP/CNHS and TGA analysis of the bulk and EDX analysis of individual crystals.

Sample	ICP/CNHS				TGA	EDX		Experimental formula
	Mg/Al	Al/Fe	C (wt%)	H (wt%)	H_2O (wt%)	Mg/Al (at.%)	Al/Fe (at.%)	
MgAl-FcMono	2.0	0.9	29.2	4.0	11.4	2.0	1.1	$Mg_2Al(OH)_6[FcMono]$ x 3.6H_2O
MgAl-FcDi	2.0	2.1	20.4	3.9	8.5	2.0	2.2	$Mg_2Al(OH)_6[FcDi]_{0.5}$ x 2.4 H_2O

Batteries & Supercaps

Research Article
doi.org/10.1002/batt.202400256

**Chemistry
Europe**
European Chemical
Societies Publishing

The characteristic pics of the C=O (1700 cm^{-1}) and C=C (1480 cm^{-1}) molecules are also visible in the HDL-FcMono and Fc—Di material. In comparison with the raw molecules the characteristic band of the C=C bond is not affected by the introduction of the molecule into the HDL phase. However, the characteristic peak of the C=O bond is shifted towards lower wavenumbers, indicating interaction with the layers and therefore its intercalation.[100]

The region between 450 and 1100 cm^{-1} represents the vibrational bands of the metal-hydroxyl bonds in the film, coupled with the release modes of the inter lamellar water molecules.

SEM images (Figure 3) shows the formation of small particles in the range of 100 nm and high-resolution TEM images (Figure 4) clearly highlight the multilayer nature of these nanoparticles, formed by corrugated stacked sheets.

MgAl-FcMono and MgAl-FcDi based electrodes were tested in two different electrolytes, which differ significantly in their chemical-physical properties. As presented in Figure 5A at 23 °C, the aqueous electrolyte 1 M LiTFSI in H$_2$O displays a very low viscosity of 0.78 mPa s. At the same time, the ionic liquid electrolyte Pyr$_{13}$TFSI has a very high viscosity of 63 mPa s (at 25 °C) without any solvent. These values have of course a strong impact on the mobility of dissociated ions in the electrolytes, which determines the ionic conductivity displayed in Figure 5B. While in 1 M LiTFSI in H$_2$O 22 mS cm^{-1} have been measured at 23 °C, Pyr$_{13}$TFSI has a much lower electrolyte conductivity of 1.4 mS cm^{-1} (at 25 °C).[101,102] Therewith, significant differences in the electrochemical performance of MgAl-FcMono and MgAl-FcDi are to be expected in the two chosen electrolytes, especially with regard to power capability (response in limited time) and cycling stability.

The first electrochemical results of MgAl-FcMono and MgAl-FcDi based electrodes tested in 1 M LiTFSI dissolved in H$_2$O are summarized in Figure 6. To begin with, Figure 6A and B present cyclic voltammograms (CVs) of both materials at 1 mV s^{-1} for 10
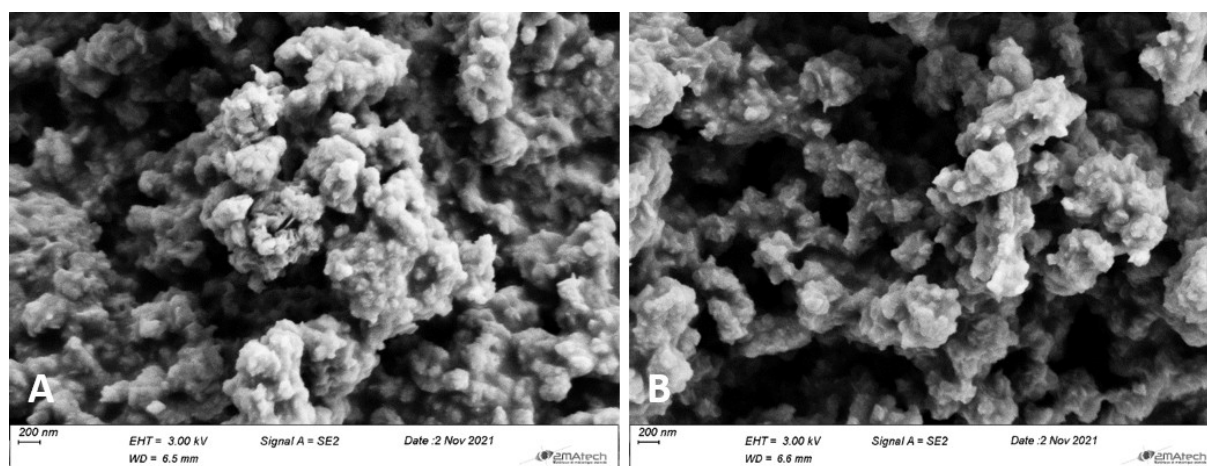

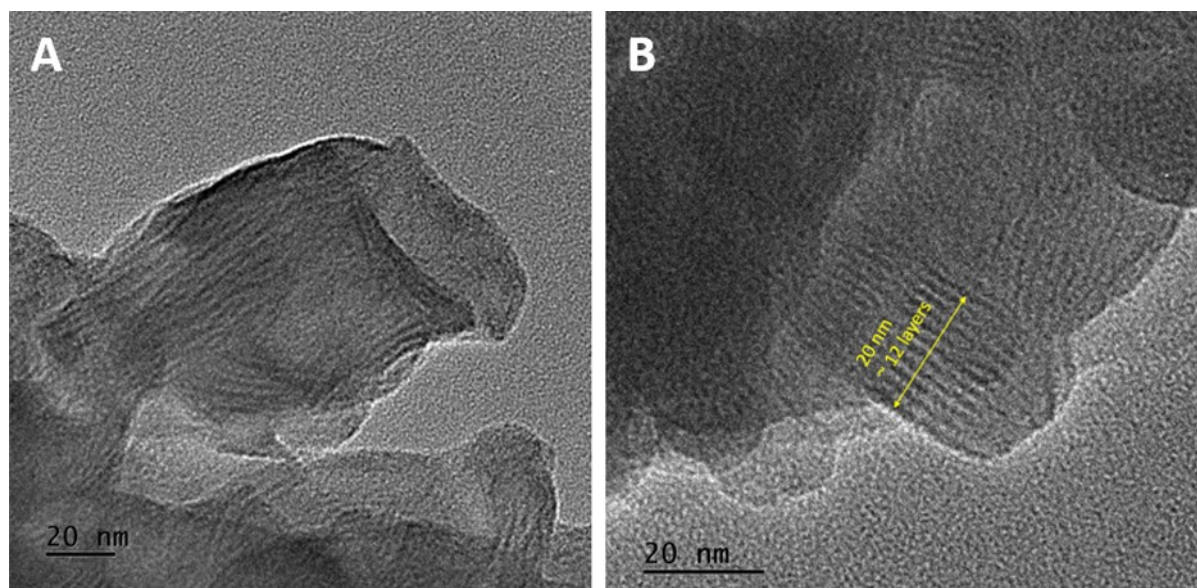**Figure 3.** SEM images of (A) MgAl-FcMono and (B) MgAl-FcDi.
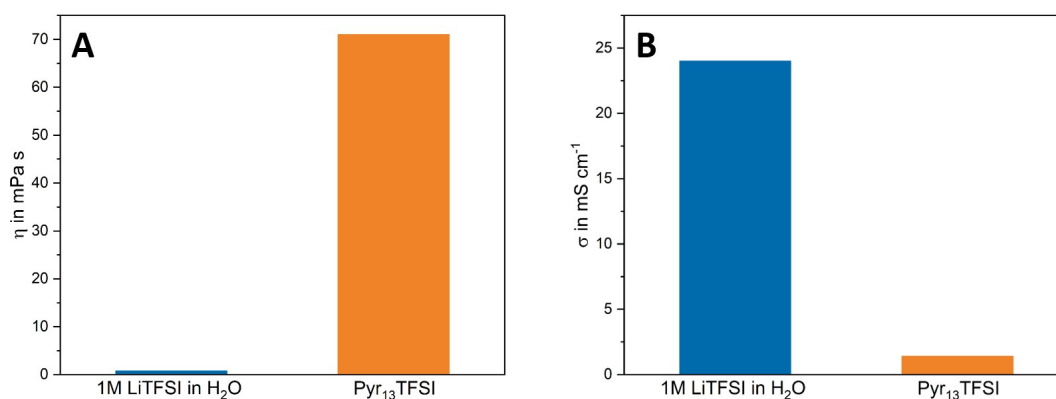

Figure 4. TEM images of (A) MgAl-FcMono and (B) MgAl-FcDi.

Figure 5. A) Viscosity and B) Conductivity of 1 M LiTFSI in H_2O and $Pyr_{13}TFSI$ at room temperature; values for $Pyr_{13}TFSI$ taken from Ref.[101].

cycles in the voltage range of -0.1–0.7 V vs. Ag. In the first cycle, the MgAl-FcMono-based electrode shows an oxidation peak at 0.58 V vs. Ag with an oxidation charge calculated from the peak area of 38.1 $mAh\,g^{-1}$. The following reduction takes place at 0.3 V vs. Ag with a reduction charge of 20.6 $mAh\,g^{-1}$, thus resulting in a coulombic efficiency of only 54%. Nevertheless, with these results the redox activity of the intercalated FcMono anions in the LDH structure of $Mg_2Al(OH)_6$ is confirmed. However, with ongoing cycling a decrease in peak intensity and thus in the stored charge is observed. At the 10th cycle, in the oxidation and reduction, a charge of 17.7 $mAh\,g^{-1}$ and 11.7 $mAh\,g^{-1}$ with a coulombic efficiency of 66% are measured. This loss in capacity indicates a decrease in the number of redox active sites of the electrode.

The same experiments were performed with MgAl-FcDi based electrodes in the same conditions (Figure 6B). In the first CV cycle, the oxidation peak is obtained at a potential of 0.64 V vs. Ag and a capacity of 33.6 $mAh\,g^{-1}$. In the corresponding reduction scan, this capacity drops to 20.5 $mAh\,g^{-1}$ with a peak at 0.22 V vs. Ag. This results in a coulombic efficiency of 66% for the first cycle. The change in redox plateau potential could be explained by additional electron withdrawing effects of the second carboxylic group. Notably, for both the main oxidation and reduction peaks a shoulder or second peak can be observed. For the oxidation, this is visible at 0.4 V vs. Ag, while for the reduction, a peak at 0.13 V vs. Ag is observed. This peak splitting could be caused by the presence of Fc–Di anions in different arrangements in the LDH structure. For example, they could be present in the discussed pillar arrangement where both anionic groups are coordinated towards the positive LDH layers (Figure 1). Next to that, also FcDi anions where only one of the groups is directly attached to the LDH can be envisioned. In such case, the electron withdrawing effect of the positive cations on the redox active ferrocene would shift the redox potential of the redox reaction in two different ways depending on whether one or two withdrawing groups are present next to the anion. This interpretation can also explain why no peak splitting is obtained during the use of MgAl-FcMono. Since, only one carboxylate group is present, there is only one possible arrangement for the intercalated anions in MgAl-

FcMono and thus only one redox potential for the redox reaction of ferrocene.

The 10th cycle of CV at 1 mVs^{-1} delivers a capacity of 20 $mAh\,g^{-1}$ from the oxidation of FcDi and 17 $mAh\,g^{-1}$ for the subsequent reduction ($\eta=85\%$). This means that for MgAl-FcDi there is also a loss in capacity over 10 cycles, which is, however, not as pronounced as for MgAl-FcMono.

A similar decrease in specific capacity is seen in the voltage vs. capacity profiles of Figure 6C and D. The electrodes were cycled over 200 galvanostatic charge/discharge in 1 M LiTFSI in H_2O at the current density corresponding to 1 C cycling rate (charge or discharge of the electrode in 1 hour assuming the full theoretical capacity of the active material). During charge of the MgAl-FcMono, 66 $mAh\,g^{-1}$ are stored in the electrode, which is surprisingly a higher value than the theoretical capacity of 56.7 $mAh\,g^{-1}$. Charge/ Discharge cycling of compositional identical $Mg_2Al(OH)_6$ based electrodes with intercalated redox-inactive octane sulfonate at 0.2 mA in 1 M LiTFSI in H_2O revealed a capacity of 0.2 $mAh\,g^{-1}$ (see S2). Therefore, the additional 9.3 $mAh\,g^{-1}$ can not be attributed to other components of the electrode like the conductive additive. Another explanation would be the presence of more ferrocene than assumed. However, EDX and ICP/CNHS measurements confirmed the correct number of intercalated ferrocene anions in $Mg_2Al(OH)_6$ (1 per unit).

Apart from that, a decrease of the molar mass of the active material MgAl-FcMono could explain the increase in capacity. For instance, it is possible that during electrode fabrication the intercalated H_2O molecules are removed via suspending of the material in ethanol and subsequent drying (see experimental part). Assuming that all water molecules are removed, the sum formula of MgAl-FcMono results to $Mg_2Al(OH)_6[FcMono]_{1.0}$ and a molar mass of 407.7 $g\,mol^{-1}$ is achieved. This lower molar mass yields to a higher theoretical capacity of 65.7 $mAh\,g^{-1}$, which aligns perfectly with the measured value of 66 $mAh\,g^{-1}$. Therefore, we can assume that $Mg_2Al(OH)_6[FcMono]_{1.0}$ is present as active material in the working electrodes.

In the discharge process, the measured capacity reduces to 16 $mAh\,g^{-1}$, which is equivalent to a coulombic efficiency of 24%. Therewith, a large loss in available active sites between the first oxidation and subsequent reduction at the working
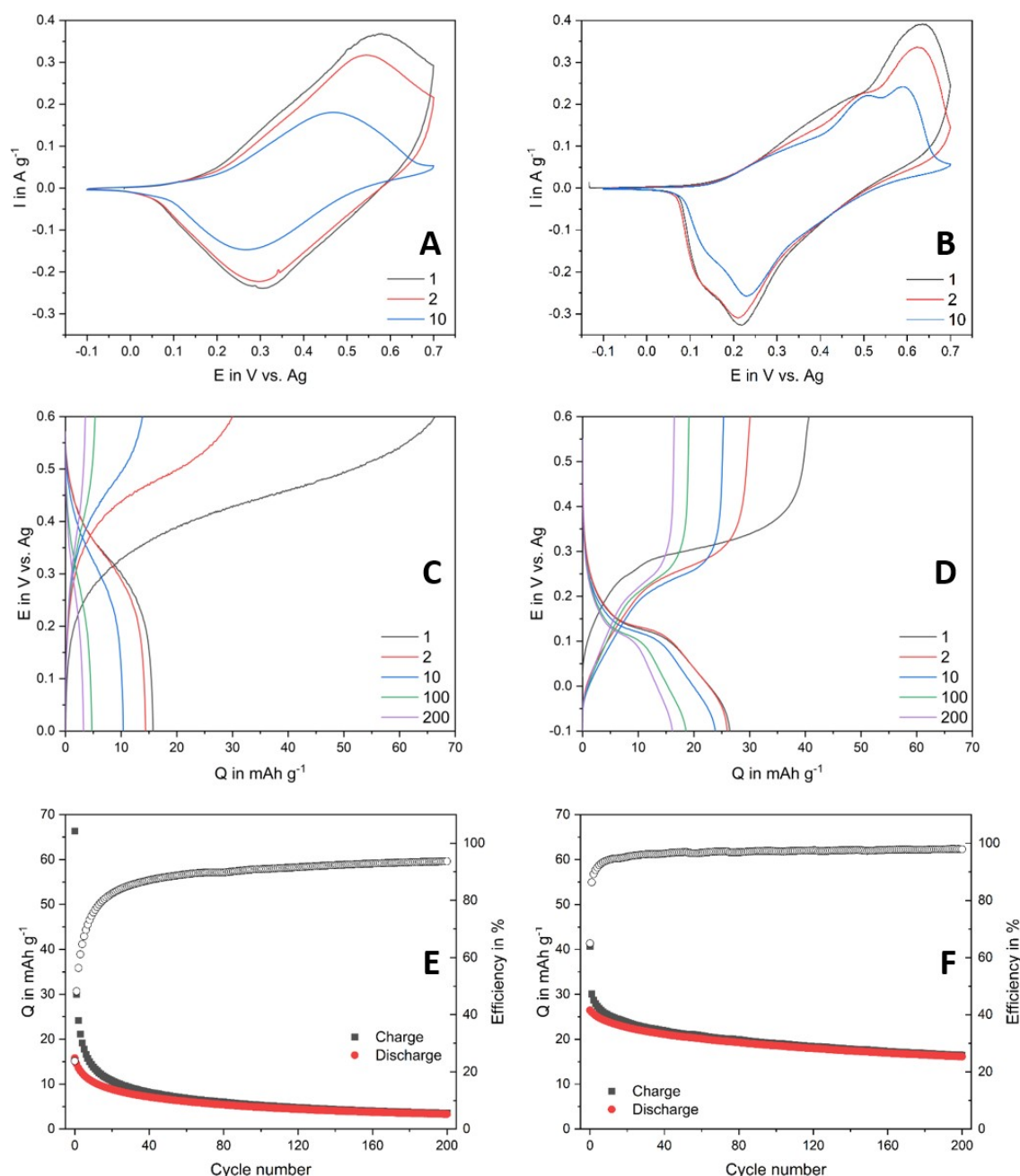
Figure 6. Cyclic voltammograms for A) MgAl-FcMono and B) MgAl-FcDi in 1 M LiTFSI in H_2O at 1 mV s^{-1}, Voltage profiles for C) MgAl-FcMono and D) MgAl-FcDi in 1 M LiTFSI in H_2O at 1 C, Cycling Stability for E) MgAl-FcMono and F) MgAl-FcDi in 1 M LiTFSI in H_2O at 1 C.

electrode is evident and indicates an irreversible charge storage. In the second charge, this loss in capacity in not recovered as the charge and discharge capacities result in 30 and 15 mAh g^{-1} respectively ($\eta = 50\%$). This decrease in specific capacities continues until the 200th cycle, where only 3 mAh g^{-1} are accessible for charge storage or delivery, which is 5% of the initial capacity observed in the first charge.

In Figure 6D the MgAl-FcDi based electrode, displays a specific capacity of 40.5 mAh g^{-1} in the first charge, which is again higher than the theoretical value of 37.5 mAh g^{-1}.

If the same logic of released H_2O molecules out of the MgAl-FcDi is applied, as it was done for MgAl-FcMono before,

the molar mass of MgAl-FcDi is 313.7 g mol^{-1}. With this species present in the working electrodes of Figure 6D, the theoretical capacity results to 42.7 mAh g^{-1}, which is even higher than the experimental value of 40.5 mAh g^{-1}. With this difference in charge, it is possible to expect a number of H_2O molecules between the initial experimental value of 2.4 and the proposed absence of H_2O in the structure of MgAl-FcDi. To calculate this number of H_2O molecules, Equation (1) can be rearranged to

$$M = \frac{z \times F}{Q_{exp} \times 3.6} \tag{2}$$

Batteries & Supercaps

Research Article
doi.org/10.1002/batt.202400256

Chemistry
Europe

European Chemical
Societies Publishing

Where Q_{exp} is the initially measured experimental capacity during the first charge. With the measured capacity of 40.5 mAh g^{-1}, a molar mass of 330.9 g mol^{-1} is obtained. When this value is subtracted from the assumed value of 357 g mol^{-1} (Mg$_2$Al(OH)$_6$[FcDi]$_{0.5}$ x 2.4 H$_2$O) a difference in molar mass of 26 g mol^{-1} is calculated, which corresponds to the molar mass of 1.4 x H$_2$O. Thus, it is possible that 1.4 x H$_2$O molecules per unit of Mg$_2$Al(OH)$_6$[FcDi]$_{0.5}$ x 2.4 H$_2$O have left the structure during electrode preparation. Therewith, for the MgAl-FcDi based electrodes Mg$_2$Al(OH)$_6$[FcDi]$_{0.5}$ x H$_2$O can be assumed as the active material of the working electrodes.

The first discharge reaches 27 mAh g^{-1}, which represents a coulombic efficiency of 67% and is by far more reversible than the first cycle presented in Figure 6C for MgAl-FcMono. The second cycle also shows a decrease in capacity; while the charging process results in 30 mAh g^{-1}, the discharge delivers a capacity of 26 mAh g^{-1} ($\eta = 87\%$). This also represents a noticeable improvement in reversibility compared to the second cycle of MgAl-FcMono. However by the 200th cycle, the specific capacity of the electrode decreased further during cycling until capacity values of 17 (charge) and 16 (discharge) mAh g^{-1} are reached ($\eta = 94\%$). Based on these results, it is obvious that both electrodes experience a drastic fade in specific capacity over the course of 200 cycles at 1 C. However, clear differences in the slopes of this decrease are visible. This is highlighted in Figure 6E and F, which present the corresponding capacities and coulombic efficiencies of MgAl-FcMono and MgAl-FcDi. From these comparisons, it may be emphasized that the electrode using MgAl-FcDi undergoes a much slower capacity fade associated with a much longer cycle life. For MgAl-FcDi the specific charge capacity falls from an initial capacity of 40.5 mAh g^{-1} to 17 mAh g^{-1}, which depicts a capacity retention of 42% after 200 cycles. On the other hand, MgAl-FcMono decreases from 66 to 3 mAh g^{-1} with a capacity retention of only 5% after 200 cycles. Moreover, most of the capacity loss occurs upon the first 10 cycles. These results suggest that much more redox active anions are stable and usable for energy storage in the structure of MgAl-FcDi than in MgAl-FcMono. A possible explanation would be a stronger interaction of the divalent anions with the positive LDH layer structure.

During the described cycling experiments, a coloration of the electrolyte was visible, departing from the working electrode vicinity. The dissolved material was identified via UV/vis spectroscopy as the formerly intercalated ferrocene anions. A dissolution of active material into the electrolyte could evidently explain the loss of capacity and insufficient cycle life described above. To investigate this phenomenon further, we quantified the dissolution of the anions upon time via in-situ UV/vis experiments. The results are presented in Figure 7.

Figure 7 shows the percentage of ferrocene anions left in the LDH structure of MgAl-FcMono and MgAl-FcDi based electrodes, with respect to the initial calculated amount in mol based on the measured mass of each electrode. The loss of redox active anions is shown in Figure 7A and B after 110 min after leaving the electrode at open circuit potential (OCP) and after 4 cycles of CV at 1 mV s^{-1} in a cuvette type cell setup with

5 ml of 1 M LiTFSI in H$_2$O electrolyte. In the case of MgAl-FcMono (Figure 7A), there is a large difference between the amount of monocarboxylic ferrocene anions dissolved in the electrolyte in OCP condition or during CV cycling. Whilst in the OCP experiment, the initial percentage of ferrocene anions in the working electrode drops from 96% to 84% after 110 min of resting in the electrolyte, this values drops down from 92% to 50% after 4 cycles in CV (107 min). Furthermore, the fact that the initial number of anions in the electrode was found to be less than 100% for both electrodes indicates that already before any oxidation, there is a dissolution of redox-active anions when the electrode is simply in contact with the electrolyte. In addition, not only the initial and final percentages are of interest, but also its evolution as shown in Figure 7A. For the OCP experiment, after a short plateau, the steepest slope for release of anions can be found in the first 20 min. Afterwards, the rate slows down and ends in a slow steady decrease in percentage. For the CV experiment, a completely different behavior can be observed.

In the first 10 min of the CV experiment (when the electrode reaches the first oxidation peak), Figure 7E shows a relatively small decrease in the amount of Fc-anions in the working electrode, down to 86%. After 10 min as the CV continues its oxidation cycle, there is the most significant drop to 56% of leftover active Fc-anions, which happens until minute 22 (the first reduction peak), after which a slight increase of Fc-anions in the electrode can be seen to 57% at 38 min (which corresponds to the second oxidation peak). Between minute 38 and 46 another steep diminution to 50% is observed (Figure 7C) which is then followed by an increase to 52% at 65 min. The described phenomenon of strong loss of Fc-anions and slight recovery repeats itself another time on the next cycle from minutes 66 to 93. This behavior is monitored three times in a cyclic manner (in line with the cyclic voltammograms), where the amount of anion loss into the electrolyte and recovery into the electrode diminishes with each cycle.

Electrodes hosting intercalated FcDi anions display a very different behavior (Figure 7B). The electrode during open circuit starts at a value of 100% of anions in the LDH structure of the electrode. Again, the most significant release of anions is visible in the first 20 min of the OCP experiment to a value of 96%. Then, there is only a slow decrease to 93% after 110 min.

For the CV at 1 mV s^{-1}, four areas with different slopes of Fc-anion decrease can be seen (Figure 7D). The first is present in the first 6 minutes before any redox activity, with a loss from the initial 98 to 96%. The second runs from 6 to 22 min until a value of 95% is reached. The next significant dissolution is seen until 30 min where 93% of anions are left in the electrode. For the rest of the experiment, there is a slow linear decrease of the Fc-anion electrode content to a final value of 90%. Importantly, it can be seen that for the OCP as well as CV experiment, higher initial and end values of divalent Fc-anions are found in the electrodes than for the monovalent one, since the general slope of anion decrease is much slower in Figure 7B compared to Figure 7A. There is less dissolution of intercalated divalent Fc-anions into the electrolyte than for monovalent ferrocene
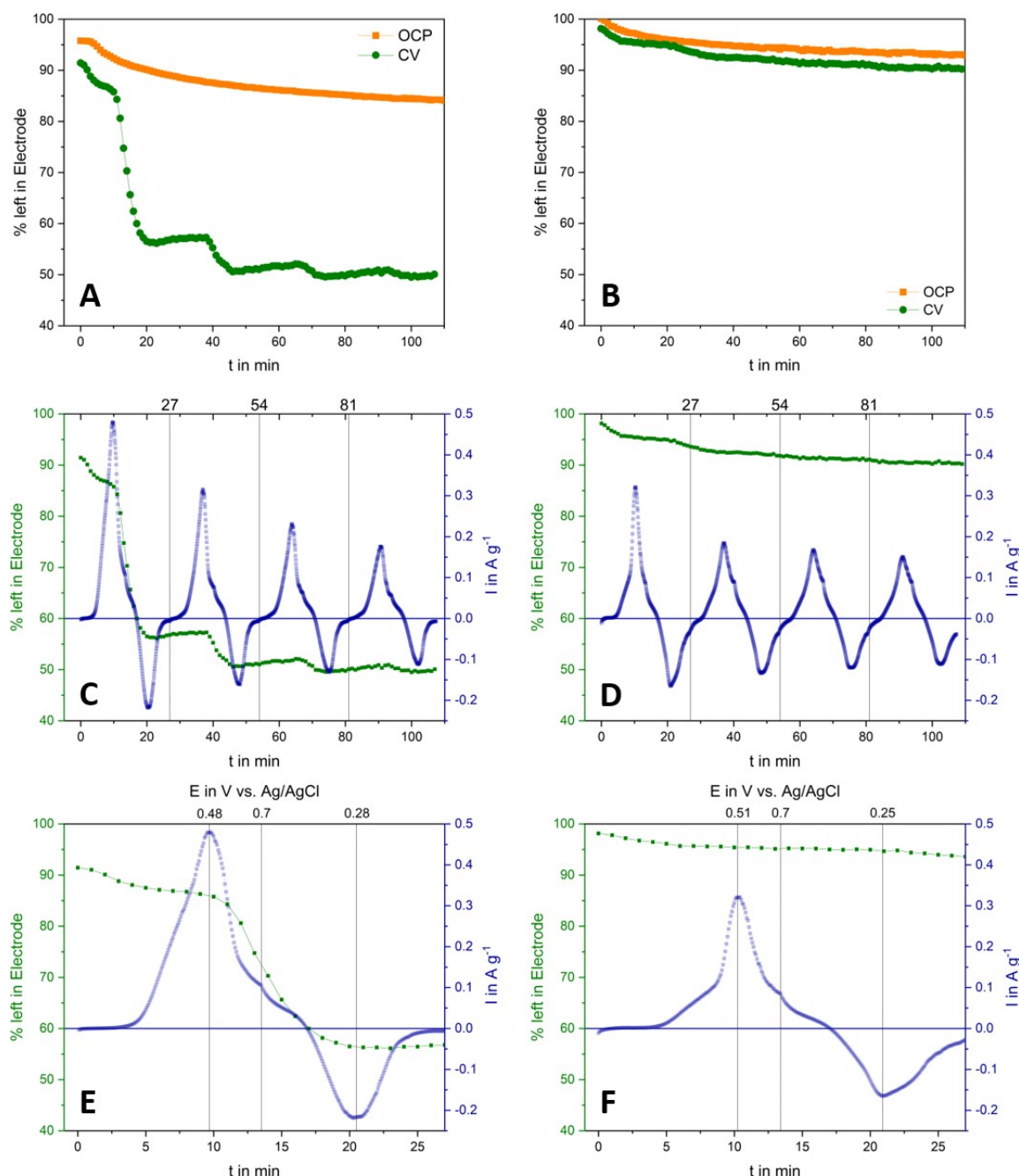
Batteries & Supercaps

Research Article
doi.org/10.1002/batt.202400256

Chemistry Europe
European Chemical
Societies Publishing

Figure 7. A) In-situ UV/vis measurements of A) MgAl-FcMono and B) MgAl-FcDi in 1 M LiTFSI in H_2O at 1 mV s^{-1}, Anion percentage evolution with overlaid unfolded CV for C) MgAl-FcMono and D) MgAl-FcDi in 1 M LiTFSI in H_2O during 4 CV cycles at 1 mV s^{-1}, Zoom in on first CV cycle for E) MgAl-FcMono and F) MgAl-FcDi.

anions. This indicates a higher stability of intercalated FcDi anions in the LDH structure of $Mg_2Al(OH)_6$.

In order to elucidate this behavior further, Figure 7C and D display the loss of Fc-anions during the CV experiments, which have been discussed already in Figure 7A and B, overlaid with the associated unfolded current measured with respect to the time from the CV plots.

From Figure 7D it is clear that the loss of Fc-anions during the CV can be correlated to the oxidation and reduction and the associated current density evolution of the four CV cycles.

For instance, the most significant loss of Fc-anions from the working electrode at 10 min, starts almost exactly at the same time as the maximum of the oxidation peak of the first CV cycle. At the 22nd minute, where the release of Fc-anions is stopped and a slight regain is measured, the reduction of the ferrocene redox couple is found. This pattern of cycle 1 (0–27 min) is found as well for cycle 2 (27–54 min), 3 (54–81 min) and 4 (81–107 min). At the same time, a similar periodicity for the release of ferrocene anions cannot be observed for dicarboxylic ferrocene anions in MgAl-FcDi based electrode (Figure 7D).

For better visibility, Figure 7E and F show a zoom-in of cycle 1 of the UV/vis experiment, which happens between minutes 0–27. In Figure 7E, it is highlighted that both changes in the slope of the percentage curve are occurring at the two extreme values of the current density curve. The loss of Fc-anions occurs at the oxidation potential of 0.48 V vs. Ag/AgCl, while the increase of Fc-anions at the electrode (due to reintercalation in the electrode or adsorption on the electrode surface) happens during the reduction at 0.28 V vs. Ag/AgCl. The electrode was subjected to a maximum potential of 0.7 V vs. Ag/AgCl in oxidation during the CV. This behavior indicates as a result of the oxidation of the monocarboxylic ferrocene anions, an instability in the LDH structure of MgAl-FcMono is created. A possible explanation for this instability could be a charge imbalance after the oxidation of ferrocene. In the uncharged state, the monovalent anions compensate the negative charge of the LDH layers. After the oxidation, the ferrocene anion bears a net neutral charge, $[Fc]^+$–COO^-. To achieve again charge neutrality in the LDH structure, anions from the electrolyte are probably inserted during this process. At the same time, since there is no interaction between the charge neutral $[Fc]^+$–COO^- and positive metal hydroxides after the oxidation, Fc-anions are released from the electrode into the electrolyte.

In Figure 7F, on the other hand, a rather constant release of anions independent from the redox current flow is measured.

No specific changes in the slope of the percentage curve are shown at the oxidation potential of 0.51 V vs. Ag/AgCl and the reduction at 0.25 v vs. Ag/AgCl. In this case, the FcDi anion, which has two carboxylates, still bears a one negative charge after the one electron oxidation. Therefore, it is possible that FcDi remains anchored to the LDH thanks to its remaining negative charge, and it is not dislodged by incoming $[TFSI]^-$ anions from the electrolyte. Thereby, the dissolution of charged FcDi is inhibited and the cycling stability of MgAl-FcDi is increased. The dissolution of charged anions into the electrolyte is illustrated in Figure 8.

Due to the results shown in Figures 6 and , it was decided to change the electrolyte media for both MgAl-FcMono- and MgAl-FcDi-based electrodes in order to reduce the possibility of dissolution of anions into the electrolyte. Next to other strategies,[103,104] Ionic liquids have often been reported to hinder the dissolution of redox active groups into the electrolyte.[105,106] Therefore, in this work we tested $Pyr_{13}TFSI$ as neat electrolyte for MgAl-FcMono and MgAl-FcDi. The results of this approach are shown in Figure 9.

The CVs in Figure 9A and B are significantly different from those displayed in Figure 6. The first CV cycle of MgAl-FcMono-based electrodes at 1 mV s^{-1} in Figure 9A presents a strong redox peak separation. The oxidation peak of the ferrocene anion is found at 0.82 V vs. Ag, whilst the reduction peak occurs
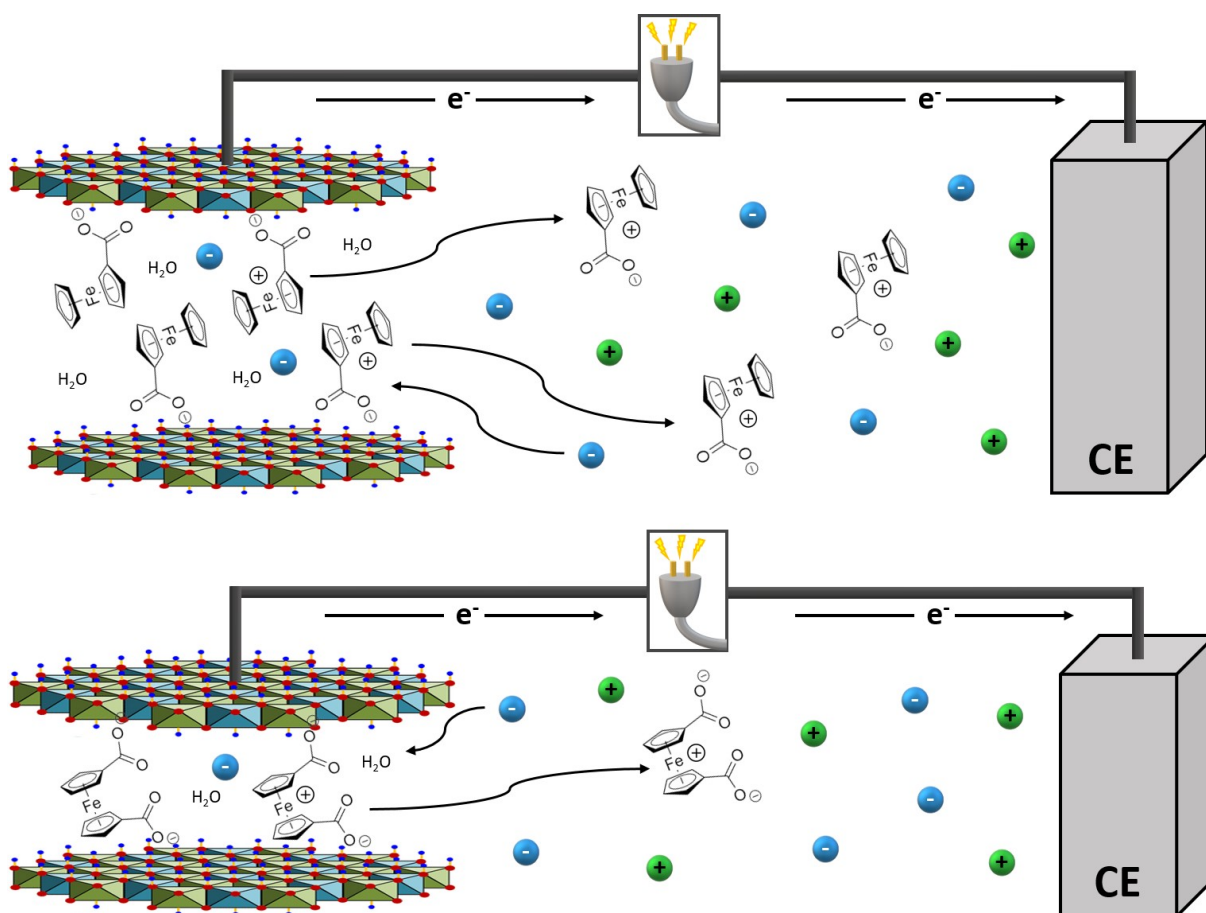

Figure 8. Schematic illustration of the dissolution of ferrocene anions into the electrolyte during the charging process for MgAl-FcMono and MgAl-FcDi.
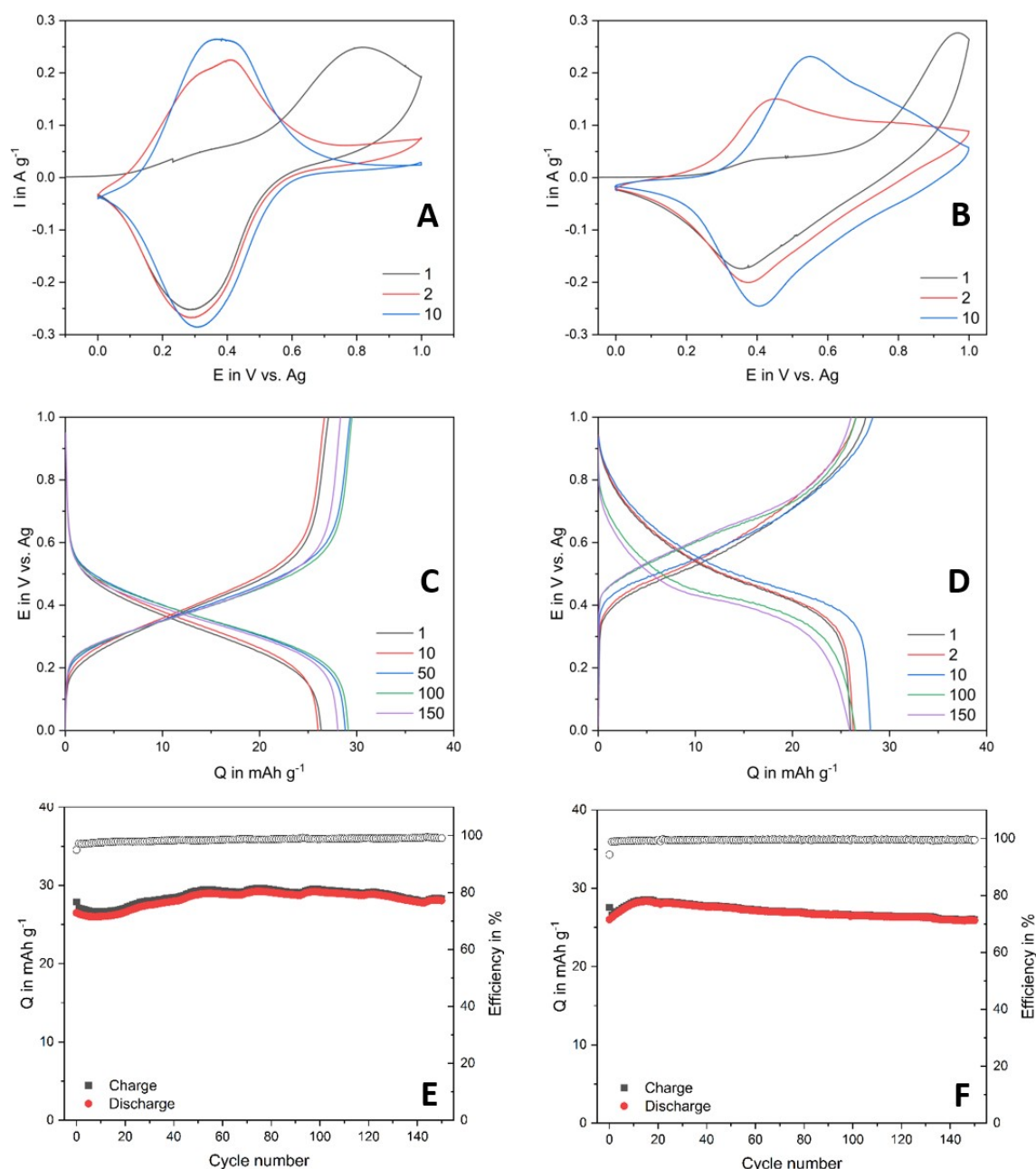
Figure 9. Cyclic voltammograms for A) MgAl-FcMono and B) MgAl-FcDi in Pyr$_{13}$TFSI at 1 mV s^{-1}, Voltage profile for C) MgAl-FcMono and D) MgAl-FcDi in Pyr$_{13}$TFSI at 1 C, Cycling stability for E) MgAl-FcMono and F) MgAl-FcDi in Pyr$_{13}$TFSI at 1 C.

at 0.3 V vs. Ag. The corresponding capacity results to 32 mAh g^{-1} for the oxidation and 29.7 mAh g^{-1} for the reduction. This yields to a coulombic efficiency of 93%, which is superior in value with respect to 54% in the aqueous electrolyte. This gain in coulombic efficiency indicates already that the dissolution of redox active anions is reduced by the utilization of the IL media. However, this is accompanied by a small decrease in specific capacity of the redox process. Furthermore, with these reported potentials, the oxidation and reduction are separated by more than 0.6 V, which denotes a high resistance in the cell. However, already in the 2nd cycle, the potential of the oxidation peak is reduced to 0.38 V vs. Ag, while the

reduction stays centered at 0.3 V vs. Ag, which represents a reversible redox behavior. A wetting process, caused by the high viscosity of the IL electrolyte, could explain this behavior. The first oxidation facilitates the wetting of the electrode and electrolyte penetration. Remarkably, the oxidation and reduction of cycle 10 display a charge of 27.5 and 27.1 mAh g^{-1} ($\eta =$ 99%). Thus, over the course of 10 cycles there is only a small decrease in peak intensity and capacities. This proves that there is no significant dissolution of active moieties into the electrolyte comparable to the aqueous system. Figure 9B shows a similar behavior. The first oxidation of the dicarboxylic ferrocene takes place at 0.97 V vs. Ag with a capacity of 20 mAh g^{-1}. The

corresponding reduction is found at 0.36 V vs. Ag with a capacity of 23 mAh g^{-1}. The higher reduction capacity (discharge) can be explained by the strong peak separation of 0.6 V, which does probably not represent the oxidation of all available active sites at the given potential window. However, this is again overcome in the 2nd cycle. At the 10th cycle, with 27.1 mAh g^{-1} for the oxidation and 27 mAh g^{-1} for the reduction, an increase in the capacity is observed. Therefore, it can be assumed that no significant dissolution of redox active anions is occurring in the IL electrolyte. The wetting process of the viscous electrolyte and the other cell components causes the increase in capacity over cycling.

The voltage profiles of Figure 9C and D suggest a similar interpretation. They show 150 charge/discharge cycles of the MgAl-FcMono- and MgAl-FcDi-based electrodes at 1 C. This time, both electrodes display a very constant cycling performance. In Figure 9C, the first charge and discharge results in a specific capacity of 28 and 26 mAh g^{-1} ($\eta = 96\%$). After 150 cycles, there is small increase to 28.5 and 28 mAh g^{-1} obtained, which can be explained by the wetting process happening inside the electrode. Figure 9D performs similarly with 28 mAh g^{-1} for the first charge and 26 mAh g^{-1} for the first discharge ($\eta = 93\%$). These values are also maintained after 150 cycles. This behavior of both MgAl-FcMono and MgAl-FcDi supports the former observations of reduced dissolution of ferrocene anions out of the electrode leading to higher cycling

stability. The overall smaller values of specific capacities are explained by the reduced conductivity of Pyr$_{13}$TFSI compared to 1 M LiTFSI in H$_2$O at room temperature. Therefore, it is possible that in the given charge time frame of 1 h (due to 1 C), not all active sites can react. Reduced current density should lead to an increase in specific capacity and therewith more redox active ferrocene in the electrodes.

For an overview of the cycling performance, Figure 9E and F display the corresponding specific capacities to Figure 9C and D with respect to the cycle number. There, a stable cycling behavior with discharge capacity retentions of 108% for MgAl-FcMono (higher than 100% due to wetting) and 96% for MgAl-FcDi with high coulombic efficiency values near 100% are observed.

It is obvious that the utilization of the IL electrolyte Pyr$_{13}$TFSI significantly improves the cycling stability of MgAl-FcMono- and MgAl-FcDi-based electrodes. This is probably achieved by the low solubility of redox active Fc-anions from the electrodes into the electrolyte due to the viscous, concentrated and ion saturated nature of the Pyr$_{13}$TFSI. To be more precise, no aqueous or organic solvent is present in this IL electrolyte to solvate the charged FcDi anions.

After these promising results, we decided to proceed with the electrochemical galvanic cycling of MgAl-FcMono and MgAl-FcDi in Pyr$_{13}$TFSI. This was done with the exact same
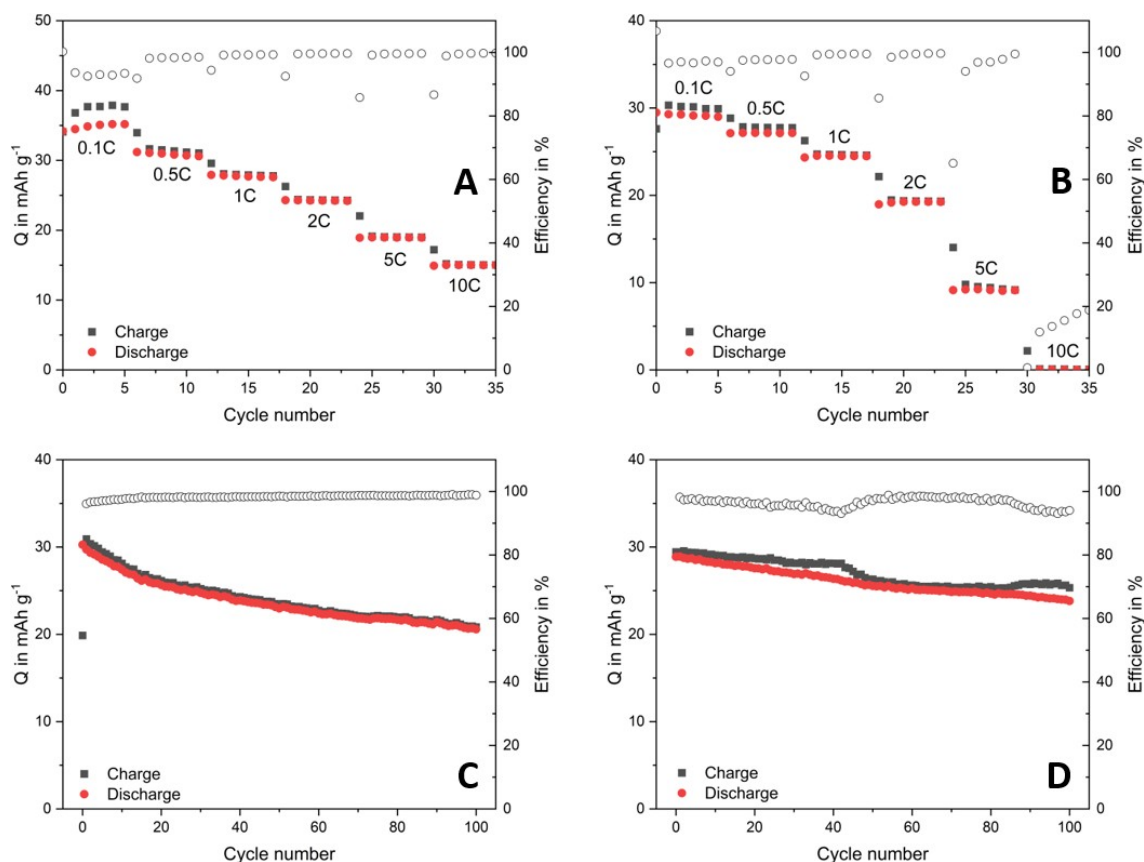

Figure 10. Rate capability for A) MgAl-FcMono and B) MgAl-FcDi in Pyr$_{13}$TFSI ranging from 0.1 to 10 C, Cycling stability for C) MgAl-FcMono and D) MgAl-FcDi in Pyr$_{13}$TFSI at 0.1 C.

Batteries & Supercaps

Research Article
doi.org/10.1002/batt.202400256

Chemistry
Europe

European Chemical
Societies Publishing

electrodes presented in Figure 9 and the results are shown in Figure 10.

Figure 10A and B display the rate capability tests of MgAl-FcMono- and MgAl-FcDi-based electrodes in the IL electrolyte in the current range from 0.1 C (charge or discharge in 10 h) to 10 C (charge or discharge in 6 min). In Figure 10A, MgAl-FcMono presents a discharge capacity of 35 mAh g^{-1} at 0.1 C. With every increase in the current density, the specific capacity decreases until at 10 C a final value of 15 mAh g^{-1} is reached (43% of the initial value at 0.1 C). This linear decrease of specific capacity with increasing current is typical for the utilization organic redox active groups in combination with viscous IL electrolytes.[105–108] At the same time, the coulombic efficiency rises from 93% at 0.1 C to close to 100% at 1 C and higher currents, suggesting less self-discharge at higher currents. The results for MgAl-FcDi are shown in Figure 10B. At 0.1 C, a specific discharge capacity of 29 mAh g^{-1} is achieved. However, with this material, the influence of current density is much more drastic than for MgAl-FcMono. When cycling at 5 C, there is a significant drop in capacity down to less than 10 mAh g^{-1}. At 10 C, there is no electrochemical response measureable at the working electrode. The reason for the faster kinetics of MgAl-FcMono in comparison to MgAl-FcDi are yet to be clarified. Except for the cycles measured at 10 C, all measurements showed a high coulombic efficiency, between 97 and 99%.

In order to verify whether the application of high currents, and the possible damage of the active materials of the composite electrodes, charge/discharge cycling stability tests at the current of 0.1 C were performed after the rate capability experiments, and they are presented in Figure 10C and D. For MgAl-FcMono-based electrodes an initial discharge capacity of 30 mAh g^{-1} is observed which is already lower than the one in Figure 10A. After 100 cycles, a specific capacity of 21 mAh g^{-1} is obtained. Thus, both initial capacity and cycling stability are reduced after the rate capability tests. This indicated electrode damage due to the stress caused by the application of high current density. In Figure 10D, MgAl-FcDi shows a discharge capacity of 29 mAh g^{-1} in the beginning of cycling, which is similar to the value obtained in Figure 10B. After 100 cycles, this value is reduced to 24 mAh g^{-1}. Therewith, MgAl-FcDi-based electrodes display an overall higher cycling stability than electrodes yielded from MgAl-FcMono.

3. Conclusions

In this work, both mono- and dicarboxylic ferrocene anions have been successfully intercalated in the structure of a Mg$_2$Al(OH)$_6$ LDH phase, which resulted to the redox active materials MgAl-FcMono and MgAl-FcDi. The intercalation was proven by means of XRD, FTIR, ICP, CHNS and TGA analysis and demonstrates an increase of interlayer space to 1.93 nm for Mg2Al-FcMono and 1.49 nm Mg2Al-FcDi, while keeping an experimental composition close to the theoretical one. These distances indicate a bilayer and a monolayer arrangement of interlayer ferrocene molecules respectively. Combined with XRD

experiments TEM-EDX analyses confirm the interlayer distances for both hybrid LDH phases.

During electrochemical tests with MgAl-FcMono and MgAl-FcDi based electrodes in the aqueous electrolyte 1 M LiTFSI in H$_2$O, both active materials showed redox activity in CV experiments and were able to store the full theoretical capacity of 60.5 mAh g^{-1} for MgAl-FcMono and 38 mAh g^{-1} MgAl-FcDi during charge at a constant current of 1 C. In both cases, however, only a fraction of this stored charge is delivered in the first discharge. This is followed by a continuous decrease in specific capacity during cycling, which is most prominent for MgAl-FcMono based electrodes. The reason for this loss in specific capacity was identified by in-situ UV/vis measurements as dissolution of charged ferrocene anions into the electrolyte 1 M LiTFSI in H$_2$O after oxidation of the electrodes. This dissolution is more severe for MgAl-FcMono than for MgAl-FcDi, due to the difference in Fc-anion charge in the oxidized state; the FcDi-anion remains negatively charge after oxidation. After the oxidation of FcMono, the intercalated anion becomes neutral and therefore does not have sufficient interaction with the surrounding positive layers of the Mg$_2$Al(OH)$_6$ LDH. In the case of MgAl-FcDi, the intercalated anions still display one negative charge after the oxidation process, which provides stronger interaction of these anions with the LDH structure and slows down the dissolution into the electrolyte. Furthermore, it was possible for the first time, to stop the dissolution by the use of the ionic liquid Pyr$_{13}$TFSI as electrolyte, which increased the cycling stability significantly. In this electrolyte, both active materials reach capacity retentions close to 100%. With these results, it is clear that both the valence of intercalated anions and the electrolyte media strongly affect the cycling stability of the tested LDHs. This additional information on the electrochemical behavior of LDHs with intercalated redox active anions will help to design new and improved candidates for this novel electrode concept in the future.

Experimental

The samples were prepared using the coprecipitation method. The synthesis reactor was pre-filled with 100 mL of ferrocene solution (0.02 M FcMono or 0.01 M FcDi) in water where the pH was adjusted to 9.5 from the start. The cation solution prepared from chloride salts (0.333 mol/L MgCl$_2$6H$_2$O and 0.167 mol/L in AlCl$_3$, 6H$_2$O) was added drop-wise (0,05 mL/min) to the reactor at 25 °C using peristaltic pumps, under magnetic stirring and a nitrogen atmosphere. 10 mL of this solution were added so that n$_{Fc}$ = 4n$_{Al}$ in the final. The pH of the reaction mixture was kept constant at 9.5 by the simultaneous addition of 1 mol/L NaOH solution. An ageing time of 24 hours was applied, after which the precipitate was recovered by three washing/centrifugation cycles and then dried in oven at 40 °C in air.

X-ray diffraction analyses were performed using a theta–theta PANalytical X'Pert Pro diffractometer equipped with a Cu anti-cathode (Kα$_1$,Kα$_2$) and an X'Celeretor detector. The X-ray patterns were recorded in the Bragg–Brentano geometry in the range of 2–80°/2θ with a step size of 0.02°.

Scanning electron microscopy (SEM) images were recorded using a JSM-7500F microscope operating at an acceleration voltage of

Batteries & Supercaps

Research Article
doi.org/10.1002/batt.202400256

Chemistry Europe
European Chemical
Societies Publishing

3 kV. Samples were deposited on conductive carbon adhesive tapes and coated with a gold thin layer.

TEM images were acquired through a JEOL 2100F microscope operating at an accelerating voltage of 200 kV. A small amount of sample was dispersed in ethanol (~2 mg/1 mL) and sonicated for 5 min. Then, a drop of the suspension was deposited on a 150 mesh Formvar carbon-coated copper grid and dried at room temperature. Local chemical composition measurements (1 nm) were performed using X-ray energy dispersion spectroscopy (XEDS) with a Jeol Si(Li) detector

Infrared spectra were recorded in transmission mode using the KBr pellet technique (2 wt %) with a Nicolet 5700 spectrometer from Thermo Scientific over the wavenumber domain of 400–4000 cm^{-1} with a scan number of 128 and a resolution of 4 cm^{-1}.

Thermogravimetric analyses (TGA) and mass spectroscopy (MS) were performed using a SETSYS Evolution de Setaram 92 coupled with a Balzers mass analyzer under air flow (20 mL/min) in the temperature range of 25–1000 °C with a linear temperature ramp of 5 °C/min.

CHNSO analysis were performed using a FlashSmart Thermo-Fisher. Samples were prepared in a tin crucible to which an oxidizing agent such as V_2O_5 was added in equal proportions. The sample was then carbonized at 900 °C (10 °C/min). The percentages of carbon, hydrogen, nitrogen and sulfur were determined using a calibration line for each element with BBOT (2,5- Bis (5-tert-butyl-benzoxazol-2-yl) thiophene, 6.1 N%, 72.53 C%, 6.09 H%, 7.44 S%).

ICP analysis were performed using an Agilent 5800 equipment. 10 mg of LDH were mineralized in a mixture of 2 mL of HCl and 6 mL of HNO_3 subjected to microwave heating at 230 °C during 30 minutes (10 °C/min, 1500 W).

The working electrodes used in this study were prepared by combing the respective LDH active material (MgAl-FcMono or MgAl-FcDi) and a carbon black conductive additive (Super Graphite, Superior Graphite Co.) in the weight ratio of 6:3 in 20 ml Ethanol (EtOH) to form a suspension. This suspension was rotated horizontally overnight in a closed glass vial with glass beads (d = 2 mm) to ensure homogenization of the two components. Afterwards the suspension was dried in an oven at 60 °C for 3 h. 10 wt % (with respect to the total mass of the dried mixture) of binder (PTFE, Sigma Aldrich) were added to the dried residue in the form of a 60 % suspension in water. This mixture was grinded in a mortar with the addition of a few drops of EtOH for 10 min to form a viscous paste, which was kneaded, rolled out and folded several times on a glass plate to create a mechanically stable sheet. After the final roll out, electrodes with a diameter of 8 mm were punched out of the sheet. After drying at 60 °C overnight, these electrodes resulted to a final area of 0.5 cm^2, a thickness of 200 μm and an average mass loading of 12 mg cm^{-2}.

For the UV/vis experiments, smaller electrodes with an average area of 0.04 cm^2 and an average mass loading of 20 mg cm^{-2} (0.831 mg average) were pressed into a stainless steel current collector in the form of a grid under 500 MPa.

The counter electrodes have been prepared as oversized self-standing carbon electrodes with a similar technique. Activated carbon (YP50, Kuaray), carbon black (Super Graphite, Superior Graphite Co.) and PTFE (Sigma Aldrich, 60 % solution) were combined in a weight ratio of 85:10:5. To this mixture, 60 ml of EtOH have been added. The suspension was stirred at 70 °C until enough EtOH had evaporated to form a viscous paste, which was afterwards transferred to a glass plate, kneaded, and folded as described above for the working electrode preparation. After the final roll out, electrodes with a diameter of 12 mm (1.13 cm^2) and a thickness of 1.3 mm were punched out. These electrodes resulted to an average mass loading of 53 mg cm^{-2}.

The investigated electrochemical cells were assembled in a 3-electrode Swagelok setup, where the working electrode was the LDH composite electrode, the counter electrode was the self-standing carbon electrode and a silver wire was used as the reference electrode. A glass fiber separator (Whatman), which was drenched with either 150 μl of 1 M LiTFSI in H_2O or neat Pyr$_{13}$TFSI as electrolyte, separated the two electrodes.

In the case of the UV/vis experiments, a different cell setup was used. Here a LDH working electrode pressed in to a stainless steel grid as current collector was submerged in 5 ml of 1 M LiTFSI in H_2O as electrolyte in a glass cuvette together with a platinum wire as counter electrode and an Ag/AgCl (3 M NaCl) electrode as the reference electrode. A magnetic stirrer was used during the experiments to provide even distribution of dissolved ions in the electrolyte.

Electrolytes were prepared by dissolving 1 M LiTFSI salt (Solvionic) in H_2O. The ionic liquid Pyr$_{13}$TFSI (Solvionic, 99, 99 %) was used neat as is. Both LiTFSI and Pyr$_{13}$TFSI were stored in a glove box (LabMaster, MBRAUN GmbH) under argon inert atmosphere with values of water and oxygen content below 0.1 ppm.

For electrolyte characterization the viscosity was measured with a rheometer (Anton Paar, MCR 72) using a shear rate of 1000 1/s, while the conductivity was determined by scanning impedance spectroscopy in the frequency range of 10 Hz to 1 MHz using a multichannel potentiostatic-galvanostatic workstation (BioLogic Science Instruments, VMP3 with ECLab software). Both measurements were carried out at 23 °C.

Electrochemical tests were performed using a multichannel potentiostatic-galvanostatic workstation (BioLogic Science Instruments, VMP3 with ECLab software) at room temperature. Before all electrochemical experiments, the cells were set to equilibrium by resting at open circuit (OCP) for 1 h.

Cyclic voltammetry (CV) experiments were exerted at a scan rate of 1 mV s^{-1}. For measurements in the aqueous electrolyte 1 M LiTFSI in H_2O a voltage window of −0.1 to 0.7 V vs. Ag was used. In the ionic liquid electrolyte Pyr$_{13}$TFSI a voltage window of 0 to 1 V vs. Ag was accessible.

Constant current galvanostatic charge/ discharge experiments were performed with a current density of 1 C. 1 C means the charge or discharge is performed within 1 h with respect to the full utilization of the theoretical capacity of the LDH active materials. For the calculation of 1 C, the molar mass of the ideal structures of $Mg_2Al(OH)_6[FcMono]_{1.0}$ x 2 H_2O and $Mg_2Al(OH)_6[FcDi]_{0.5}$ x 2 H_2O have been used. The voltage limits have been derived from CV measurements. For rate capability tests, current densities of 0.1, 0.5, 1, 2, 5, and 10 C have been used.

UV/vis analysis was carried out using a UV/Vis/NIR spectrophotometer (PerkinElmer LAMBDA 1050) in transmission mode. The absorption maximum of ferrocene in the aqueous electrolyte was located at 268 nm and absorption spectra were measured in the range between 250–300 nm.

Acknowledgements

Batteries & Supercaps

Research Article
doi.org/10.1002/batt.202400256

Chemistry
Europe
European Chemical
Societies Publishing

Conflict of Interests

The authors declare no conflict of interest.

Data Availability Statement

The data that support the findings of this study are available from the corresponding author upon reasonable request.

[1] A. I. Khan, A. Ragavan, B. Fong, C. Markland, M. O'Brien, T. G. Dunbar, G. R. Williams, D. O'Hare, *Ind. Eng. Chem. Res.* **2009**, *48*, 10196–10205.
[2] Q. Wang, D. O'Hare, *Chem. Rev.* **2012**, *112*, 4124–4155.
[3] J. Yu, Q. Wang, D. O'Hare, L. Sun, *Chem. Soc. Rev.* **2017**, *46*, 5950–5974.
[4] X. Guo, F. Zhang, D. G. Evans, X. Duan, *Chem. Commun.* **2010**, *46*, 5197.
[5] L. Li, R. Ma, Y. Ebina, K. Fukuda, K. Takada, T. Sasaki, *J. Am. Chem. Soc.* **2007**, *129*, 8000–8007.
[6] A. I. Khan, D. O'Hare, *J. Mater. Chem.* **2002**, *12*, 3191–3198.
[7] M. Duan, S. Liu, Q. Jiang, X. Guo, J. Zhang, S. Xiong, *Chin. Chem. Lett.* **2022**, *33*, 4428–4436.
[8] S. J. Mills, A. G. Christy, J.-M. R. Génin, T. Kameda, F. Colombo, *Mineral. mag.* **2012**, *76*, 1289–1336.
[9] F. Cavani, F. Trifirb, A. Vaccari, *Catalysis Today* **1991**, *11*, 173–301.
[10] C. Taviot-Guého, V. Prévot, C. Forano, G. Renaudin, C. Mousty, F. Leroux, *Adv. Funct. Mater.* **2018**, *28*, 1703868.
[11] C. Taviot-Guého, Y. Feng, A. Faour, F. Leroux, *Dalton Trans.* **2010**, *39*, 5994.
[12] A. V. Radha, P. Vishnu Kamath, C. Shivakumara, *Solid State Sci* **2005**, *7*, 1180–1187.
[13] L. Lv, P. Sun, Z. Gu, H. Du, X. Pang, X. Tao, R. Xu, L. Xu, *J. Hazard. Mater.* **2009**, *161*, 1444–1449.
[14] V. K. Ameena Shirin, R. Sankar, A. P. Johnson, H. V. Gangadharappa, K. Pramod, *J. Controlled Release* **2021**, *330*, 398–426.
[15] S.-J. Ryu, H. Jung, J.-M. Oh, J.-K. Lee, J.-H. Choy, *J. Phys. Chem. Solids* **2010**, *71*, 685–688.
[16] X. Bi, H. Zhang, L. Dou, *Pharmaceutics* **2014**, *6*, 298–332.
[17] K. Zhang, Z. Xu, J. Lu, Z. Tang, H. Zhao, D. Good, M. Wei, *Int. J. Mol. Sci.* **2014**, *15*, 7409–7428.
[18] Y. Zhao, S. He, M. Wei, D. G. Evans, X. Duan, *Chem. Commun.* **2010**, *46*, 3031.
[19] M. Sajid, S. M. Sajid Jillani, N. Baig, K. Alhooshani, *Chemosphere* **2022**, *287*, 132140.
[20] B. M. V. da Gama, R. Selvasembian, D. A. Giannakoudakis, K. S. Triantafyllidis, G. McKay, L. Meili, *Molecules* **2022**, *27*, 4900.
[21] M. Zubair, M. Daud, G. McKay, F. Shehzad, M. A. Al-Harthi, *Applied Clay Science* **2017**, *143*, 279–292.
[22] Y. Gao, J. Wu, Q. Wang, C. A. Wilkie, D. O'Hare, *J. Mater. Chem. A* **2014**, *2*, 10996.
[23] D. G. Evans, X. Duan, *Chem. Commun.* **2006**, 485–496.
[24] A. Illaik, C. Vuillermoz, S. Commereuc, C. Taviot-Guého, V. Verney, F. Leroux, *J. Phys. Chem. Solids* **2008**, *69*, 1362–1366.
[25] D. Li, F. Wang, X. Yu, J. Wang, Q. Liu, P. Yang, Y. He, Y. Wang, M. Zhang, *Prog. Org. Coat.* **2011**, *71*, 302–309.
[26] F. Zhang, L. Zhao, H. Chen, S. Xu, D. G. Evans, X. Duan, *Angew. Chem.* **2008**, *120*, 2500–2503.
[27] F. Zhang, M. Sun, S. Xu, L. Zhao, B. Zhang, *Chem. Eng. J.* **2008**, *141*, 362–367.
[28] S. K. Poznyak, J. Tedim, L. M. Rodrigues, A. N. Salak, M. L. Zheludkevich, L. F. P. Dick, M. G. S. Ferreira, *ACS Appl. Mater. Interfaces* **2009**, *1*, 2353–2362.
[29] H. Ai, X. Huang, Z. Zhu, J. Liu, Q. Chi, Y. Li, Z. Li, X. Ji, *Biosens. Bioelectron.* **2008**, *24*, 1048–1052.
[30] H. Fan, Y. Li, D. Wu, H. Ma, K. Mao, D. Fan, B. Du, H. Li, Q. Wei, *Anal. Chim. Acta* **2012**, *711*, 24–28.
[31] H. Sohrabi, O. Arbabzadeh, M. Falaki, M. R. Majidi, N. Han, Y. Yoon, A. Khataee, *Food Chem. Toxicol.* **2022**, *164*, 113010.
[32] Y. Wang, Z. Wang, Y. Rui, M. Li, *Biosens. Bioelectron.* **2015**, *64*, 57–62.
[33] B. Ballarin, M. Morigi, E. Scavetta, R. Seeber, D. Tonelli, *J. Electroanal. Chem.* **2000**, *492*, 7–14.
[34] C. Mousty, *Appl. Clay Sci.* **2004**, *27*, 159–177.
[35] D. Tang, Y. Han, W. Ji, S. Qiao, X. Zhou, R. Liu, X. Han, H. Huang, Y. Liu, Z. Kang, *Dalton Trans.* **2014**, *43*, 15119–15125.
[36] X. Long, J. Li, S. Xiao, K. Yan, Z. Wang, H. Chen, S. Yang, *Angew. Chem.* **2014**, *53*(29), 7584–7588.
[37] Z. Lei, *J. Energy Chem.* **2017**, *26*, 1094–1106.
[38] D. Tang, J. Liu, X. Wu, R. Liu, X. Han, Y. Han, H. Huang, Y. Liu, Z. Kang, *ACS Appl. Mater. Interfaces* **2014**, *6*, 7918–7925.
[39] C. Tang, H.-S. Wang, H.-F. Wang, Q. Zhang, G.-L. Tian, J.-Q. Nie, F. Wei, *Adv. Mater.* **2015**, *27*, 4524–4524.
[40] X. Chen, C. Fu, Y. Wang, W. Yang, D. G. Evans, *Biosens. Bioelectron.* **2008**, *24*, 356–361.
[41] X. Zou, A. Goswami, T. Asefa, *J. Am. Chem. Soc.* **2013**, *135*, 17242–17245.
[42] B. Ballarin, R. Seeber, D. Tonelli, A. Vaccari, *J. Electroanal. Chem.* **1999**, *463*, 123–127.
[43] E. Sca, *Electrochim. Acta* **2002**, *47*, 2451–2461.
[44] Y. Li, *J. Mater. Chem. A* **2014**, *2*, 13250–13258.
[45] F. Song, *Nat. Commun.* **2014**, *5*, 4477.
[46] H. Wang, X. Xiang, F. Li, *J. Mater. Chem.* **2010**, *20*, 3944.
[47] Z. Li, *Chem. Sci.* **2015**, *6*, 6624–6631.
[48] X. Lei, F. Zhang, L. Yang, X. Guo, Y. Tian, S. Fu, F. Li, D. G. Evans, X. Duan, *AIChE J.* **2007**, *53*, 932–940.
[49] K. Ebitani, K. Motokura, T. Mori, T. Mizugaki, K. Kaneda, *J. Org. Chem.* **2006**, *71*, 5440–5447.
[50] M. Shao, R. Zhang, Z. Li, M. Wei, D. G. Evans, X. Duan, *Chem. Commun.* **2015**, *51*, 15880–15893.
[51] E. Shangguan, H. Zhang, C. Wu, X. Cai, Z. Wang, M. Wang, L. Li, G. Wang, Q. Li, J. Li, *Electrochim. Acta* **2020**, *330*, 135198.
[52] A. B. Béléké, E. Higuchi, H. Inoue, M. Mizuhata, *J. Power Sources* **2014**, *247*, 572–578.
[53] Z. Zhang, Z. Yang, J. Huang, Z. Feng, X. Xie, *Electrochim. Acta* **2015**, *155*, 61–68.
[54] Y. Liu, Z. Yang, *RSC Adv.* **2016**, *6*, 68584–68591.
[55] J. Liu, Y. Li, X. Huang, G. Li, Z. Li, *Adv. Funct. Mater.* **2008**, *18*, 1448–1458.
[56] B. Yang, Z. Yang, R. Wang, T. Wang, *Electrochim. Acta* **2013**, *111*, 581–587.
[57] M. A. González, R. Trócoli, I. Pavlovic, C. Barriga, F. La Mantia, *Electrochem. Commun.* **2016**, *68*, 1–4.
[58] A. Sumboja, J. Chen, Y. Zong, P. S. Lee, Z. Liu, *Nanoscale* **2017**, *9*, 774–780.
[59] G. A. Caravaggio, C. Detellier, Z. Wronski, *J. Mater. Chem.* **2001**, *11*, 912–921.
[60] X. Long, Z. Wang, S. Xiao, Y. An, S. Yang, *Mater. Today* **2016**, *19*, 213–226.
[61] J. He, W. Zhou, D. Zhu, J. Li, Z. Liu, Y. Chen, *ACS Sustainable Chem. Eng.* **2020**, *8*, 14877–14885.
[62] W. Yu, N. Deng, K. Cheng, J. Yan, B. Cheng, W. Kang, *J. Energy Chem.* **2021**, *58*, 472–499.
[63] L. Shi, Y. Chen, R. He, X. Chen, H. Song, *Phys. Chem. Chem. Phys.* **2018**, *20*, 16437–16443.
[64] A. D. Deshmukh, A. R. Urade, A. P. Nanwani, K. A. Deshmukh, D. R. Peshwe, P. Sivaraman, S. J. Dhoble, B. K. Gupta, *ACS Omega* **2018**, *3*, 7204–7213.
[65] R. A. Senthil, A. Min, J. Theerthagiri, G.-A. Kim, H. C. Choi, M. Y. Choi, *J. Storage Mater.* **2023**, *72*, 108305.
[66] D. Zhang, X. Guo, X. Tong, Y. Chen, M. Duan, J. Shi, C. Jiang, L. Hu, Q. Kong, J. Zhang, *J. Alloys Compd.* **2020**, *837*, 155529.
[67] Y. Wang, H. Yang, H. Lv, Z. Zhou, Y. Zhao, H. Wei, Z. Chen, *J. Colloid Interface Sci.* **2022**, *610*, 35–48.
[68] H. Liang, J. Lin, H. Jia, S. Chen, J. Qi, J. Cao, T. Lin, W. Fei, J. Feng, *J. Power Sources* **2018**, *378*, 248–254.

Batteries & Supercaps

Research Article
doi.org/10.1002/batt.202400256

Chemistry Europe
European Chemical
Societies Publishing

[69] X. Zhao, H. Li, M. Zhang, W. Pan, Z. Luo, X. Sun, *ACS Appl. Mater. Interfaces* **2022**, *14*, 34781–34792.

[70] X. Zhang, C. B. Cockreham, E. Yılmaz, G. Li, N. Li, S. Ha, L. Fu, J. Qi, H. Xu, D. Wu, *J. Phys. Chem. Lett.* **2020**, *11*, 3745–3753.

[71] J.-J. Zhou, Q. Li, C. Chen, Y.-L. Li, K. Tao, L. Han, *Chem. Eng. J.* **2018**, *350*, 551–558.

[72] C.-S. Ni, S.-F. Liu, J.-F. Lee, C.-W. Pao, J.-L. Chen, H.-Y. Chen, J.-H. Huang, *Electrochim. Acta* **2021**, *384*, 138415.

[73] Y. Jiang, Y. Song, Y. Li, W. Tian, Z. Pan, P. Yang, Y. Li, Q. Gu, L. Hu, *ACS Appl. Mater. Interfaces* **2017**, *9*, 37645–37654.

[74] A. D. Jagadale, G. Guan, X. Li, X. Du, X. Ma, X. Hao, A. Abudula, *J. Power Sources* **2016**, *306*, 526–534.

[75] X. Liu, A. Zhou, T. Pan, Y. Dou, M. Shao, J. Han, M. Wei, *J. Mater. Chem. A* **2016**, *4*, 8421–8427.

[76] B. Wang, G. R. Williams, Z. Chang, M. Jiang, J. Liu, X. Lei, X. Sun, *ACS Appl. Mater. Interfaces* **2014**, *6*, 16304–16311.

[77] Y. Yao, H. Li, Y. Yu, C. Du, L. Wan, H. Ye, J. Chen, Y. Zhang, M. Xie, *J. Storage Mater.* **2023**, *59*, 106422.

[78] T. Brousse, D. Belanger, J. W. Long, *J. Electrochem. Soc.* **2015**, *162*, 5185–5189.

[79] C. Mousty, S. Therias, C. Forano, J.-P. Besse, *J. Electroanal. Chem.* **1994**, *374*, 63–69.

[80] S. Therias, C. Mousty, *Appl. Clay Sci.* **1995**, *10*, 147–162.

[81] J. Sarmet, F. Leroux, C. Taviot-Gueho, P. Gerlach, C. Douard, T. Brousse, G. Toussaint, P. Stevens, *Molecules* **2023**, *28*, 1006.

[82] P. Gerlach, C. Douard, I. Gaalich, L. Athouël, J. Sarmet, F. Leroux, C. Tavoit-Gueho, P. Stevens, G. Toussaint, T. Brousse, *J. Electrochem. Soc.* **2023**, *170*, 070505.

[83] M. Hu, M. Abbasi-Azad, B. Habibi, F. Rouhani, H. Moghanni-Bavil-Olyaei, K. Liu, A. Morsali, *ChemPlusChem* **2020**, *85*, 2397–2418.

[84] R. R. Gagne, C. A. Koval, G. C. Lisensky, *Inorg. Chem.* **1980**, *19*, 2854–2855.

[85] J. K. Bashkin, P. J. Kinlen, *Inorg. Chem.* **1990**, *29*, 4507–4509.

[86] J. A. M. Xavier, C. Viñas, E. Lorenzo, T. García-Mendiola, F. Teixidor, *Chem. Commun.* **2022**, *58*, 4196–4199.

[87] G. Gritzner, J. Kuta, *Pure App. Chem.* **1984**, *56*, 461–466.

[88] L. Fabbrizzi, *ChemTexts* **2020**, *6*, 22.

[89] T. Kuwana, D. E. Bublitz, G. Hoh, *J. Am. Chem. Soc.* **1960**, *82*, 5811–5817.

[90] C. Li, C. Zhang, J. Xie, K. Wang, J. Li, Q. Zhang, *Chem. Eng. J.* **2021**, *404*, 126463.

[91] C. Li, H. Yang, J. Xie, K. Wang, J. Li, Q. Zhang, *ACS Appl. Mater. Interfaces* **2020**, *12*, 32719–32725.

[92] J. Xiang, K. Sato, H. Tokue, K. Oyaizu, C. Ho, H. Nishide, W. Wong, M. Wei, *Eur. J. Inorg. Chem.* **2016**, *2016*, 1030–1035.

[93] Y. Ding, Y. Zhao, G. Yu, *Nano Lett.* **2015**, *15*, 4108–4113.

[94] P. S. Borchers, M. Strumpf, C. Friebe, I. Nischang, M. D. Hager, J. Elbert, U. S. Schubert, *Adv. Energy Mater.* **2020**, *10*, 2001825.

[95] Q. Chen, Y. Li, Y. Liu, P. Sun, Z. Yang, T. Xu, *ChemSusChem* **2021**, *14*, 1295–1301.

[96] Y. Zhen, C. Zhang, J. Yuan, Y. Zhao, Y. Li, *J. Power Sources* **2020**, *480*, 229132.

[97] Z. Zhao, B. Zhang, B. R. Schrage, C. J. Ziegler, A. Boika, *ACS Appl. Energy Mater.* **2020**, *3*, 10270–10277.

[98] H.-M. Koepp, H. Wendt, H. Strehlow, *Z. Elektrochem.* **1960**, *64*, 483–491.

[99] T. Hibino, *Appl. Clay Sci.* **2015**, *116–117*, 93–101.

[100] K. Nakamoto, *Infrared and Raman spectra of inorganic and coordination compounds, part B: applications in coordination, organometallic, and bioinorganic chemistry*, John Wiley & Sons, **2009**.

[101] J. Barisci, *Electrochem. Commun.* **2004**, *6*, 22–27.

[102] M. Galiński, A. Lewandowski, I. Stępniak, *Electrochim. Acta* **2006**, *51*, 5567–5580.

[103] Y. Li, Z. Yu, J. Huang, Y. Wang, Y. Xia, *Angew. Chem. Int. Ed.* **2023**, *135*, e202309957.

[104] Z. Zhao, W. Zhang, M. Liu, S. J. Yoo, N. Yue, F. Liu, X. Zhou, K. Song, J.-G. Kim, Z. Chen, X.-Y. Lang, Q. Jiang, C. Zhi, W. Zheng, *Nano Lett.* **2023**, *23*, 5307–5316.

[105] W. Zhang, H. Tian, J. Wang, H. Sun, J. Wang, W. Huang, *ACS Appl. Mater. Interfaces* **2022**, *14*, 38887–38894.

[106] P. Gerlach, R. Burges, A. Lex-Balducci, U. S. Schubert, A. Balducci, *J. Power Sources* **2018**, *405*, 142–149.

[107] P. Gerlach, R. Burges, A. Lex-Balducci, U. S. Schubert, A. Balducci, *J. Electrochem. Soc.* **2020**, *167*, 120546.

[108] B. Yang, C. Li, J. Zhou, J. Liu, Q. Zhang, *Electrochim. Acta* **2014**, *148*, 39–45.